Stratigraphic record reveals contrasting roles of overflows and underflows over glacial cycles in a hypersaline lake (Dead Sea)

Yin Lu [a],*, Ed L. Pope [b], Jasper Moernaut [a], Revital Bookman [c], Nicolas Waldmann [c], Amotz Agnon [d], Shmuel Marco [e], Michael Strasser [a]

[a] *Institute of Geology, University of Innsbruck, 6020 Innsbruck, Austria*
[b] *Department of Geography, Durham University, DH1 3LE Durham, UK*
[c] *Dr. Moses Strauss Department of Marine Geosciences, University of Haifa, 3498838 Haifa, Israel*
[d] *Institute of Earth Sciences, Hebrew University of Jerusalem, 91904 Jerusalem, Israel*
[e] *Department of Geophysics, Tel Aviv University, 6997801 Tel Aviv, Israel*

ARTICLE INFO

ABSTRACT

In lakes and oceans, links between modern sediment density flow processes and deposits preserved in long-term geological records are poorly understood. Consequently, it is unclear whether, and if so how, long-term climate changes affect the magnitude/frequency of sediment density flows. One approach to answering this question is to analyze a comprehensive geological record that comprises deposits that can be reliably linked to modern sediment flow processes. To address this question, we investigated the unique ICDP Core 5017-1 from the Dead Sea (the largest and deepest hypersaline lake on the Earth) depocenter covering MIS 7-1. Based on an understanding of modern sediment density flow processes in the lake, we link homogeneous muds in the core to overflows (surface flood plumes, $\rho_{\text{flow}} < \rho_{\text{water}}$), and link graded turbidites and debrites to underflows ($\rho_{\text{flow}} > \rho_{\text{water}}$). Our dataset reveals (1) overflows are more prominent during interglacials, while underflows are more prominent during glacials; (2) orbital-scale climate changes affected the flow magnitude/frequency via changing salinity and density profile of lake brine, lake-level, and source materials.

1. Introduction

Modern field measurements, laboratory experiments, and the geological record demonstrate that subaqueous sediment density flows ($\rho_{\text{flow}} < \rho_{\text{water}}$, overflows or hypopycnal flows; $\rho_{\text{flow}} > \rho_{\text{water}}$, underflows or hyperpycnal flows, including turbidity currents and debris flows) are major processes for transporting terrestrial sediments and organic carbon from rivers, coasts or continental shelves into deep basins (Sturm and Matter, 1978; Van Rooij, 2004; Lamb et al., 2010; Talling et al., 2012; Pope et al., 2017; de Leeuw et al., 2018; Zhang et al., 2018; Liu et al., 2020). It has been shown that over glacial cycles the physical and chemical properties of water bodies, water levels, and the catchment areas and sediment supply can vary greatly (Thunell and Williams, 1989; Lisiecki and Raymo, 2005; Grant et al., 2012; Torfstein et al., 2013; Lazar et al., 2014). This raises the question of whether long-term climate changes can affect the magnitude/frequency of sediment

density flows entering a specific water body, and if so what controls the variability.

One possible approach to explore these questions is by investigating a comprehensive geological record from past glacial cycles from a specific water body. However, the links between modern sediment density flows and resulting deposits in long-term geological records are poorly understood and have rarely been investigated so far (Piper and Savoye, 1993; Maier et al., 2019). This is because it is rare that both comprehensive long-term geological records (with ages well-constrained and sediment facies intensively investigated) and modern flow monitoring data are available for a specific water body.

The Dead Sea is the largest and deepest hypersaline lake (ρ_{water}: 1240 kg/m^3) on Earth. Floods and turbid water have been monitored here (Levy, 1981; Stiller et al., 1997; Herut et al., 2002; Nehorai et al., 2013), meaning these and related subaqueous sediment density flow processes are relatively well-understood. In addition, paleoenvironments in the region have been intensively investigated (Bar-Matthews et al., 2003; Torfstein et al., 2013; Miebach et al., 2019). ICDP (International Continental Drilling Program) Core 5017-1 from the hypersaline lake depocenter provides
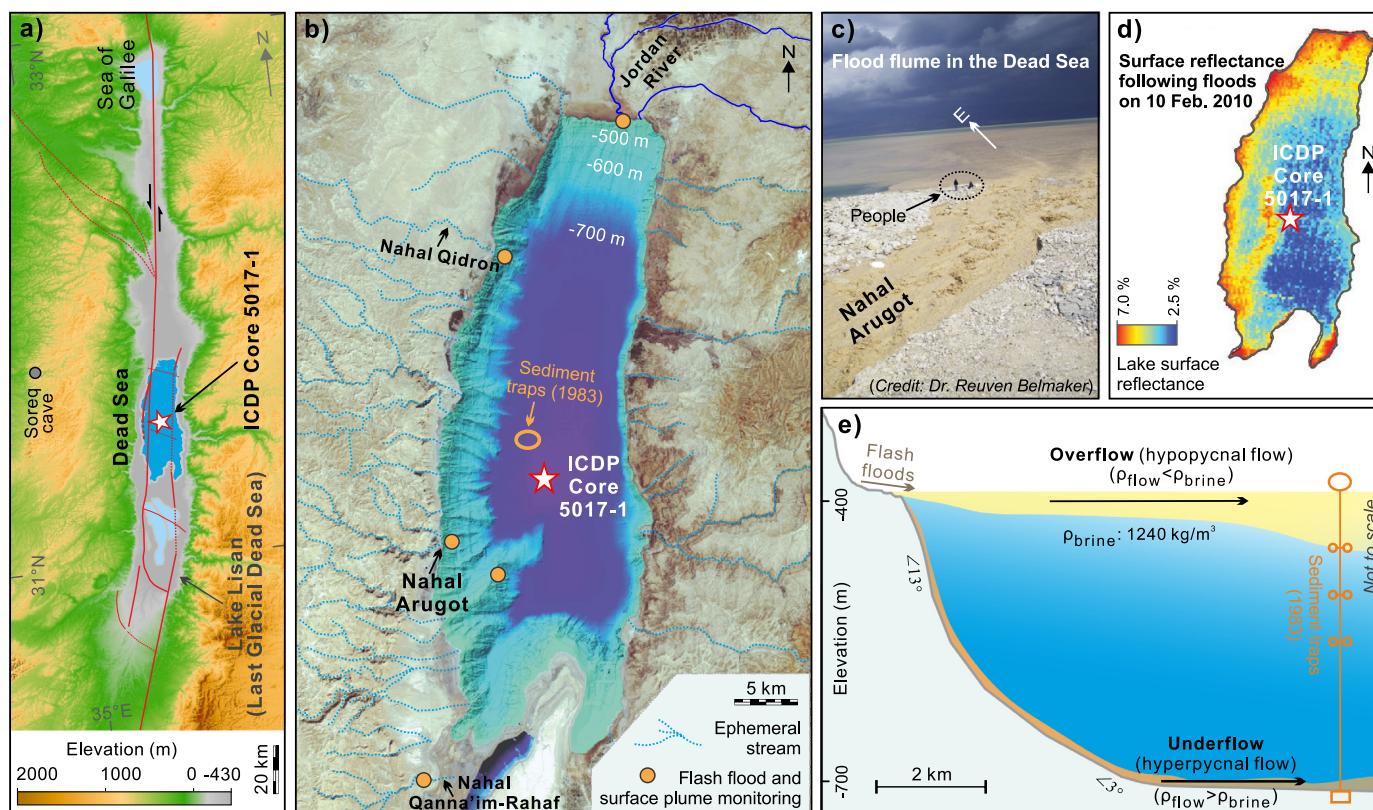
Fig. 1. Location of the ICDP Core 5017-1 and modern sediment density flow processes in the Dead Sea. a: Tectonic setting of the Dead Sea Basin (Bartov et al., 2006; Ben-Avraham et al., 2008). b: Dead Sea tributaries (Greenbaum et al., 2006). c: Flood plume observed in the western lakeshore (Nahal Arugot; Fig. 1b) (Belmaker et al., 2019). d: Lake surface reflectance (remote sensing) map of the lake following flash floods (adapted from Nehorai et al., 2013). e: Schematic model showing flow processes that may result from floods in the salty lake.

a geological record covering marine oxygen isotope stage 7-1 (MIS 7-1; 220-0 ka) (Torfstein et al., 2015; Goldstein et al., 2020). The combination of the well-constrained regional paleoenvironment around the lake and the completeness of ICDP Core 5017-1 make this record ideal for: (1) understanding the links between modern sediment density flow processes and ancient deposits; (2) detecting whether the magnitude and/or frequency of the flows are stable or not through glacial cycles; and (3) if not, revealing how the changing environment has affected the magnitude/frequency of the flows.

2. Geological setting and hypothesis

2.1. Geography of the Dead Sea

The Dead Sea Basin, the largest pull-apart basin along the Dead Sea Transform (Fig. 1a), has been occupied by a sequence of terminal water bodies during the Quaternary such as the Dead Sea (MIS 1) and Lake Lisan (MIS 4-2) (Stein, 2001). Lake Lisan, which existed during the Last Glacial Maximum, is the largest known lacustrine system (Fig. 1a), had a lake level at 180 m below mean sea-level (-180 m) and a surface area of $\sim$3200 km^2 (Hall, 1997; Torfstein et al., 2013). The Dead Sea currently has a water level at -435 m and a surface area of $\sim$600 km^2.

Climate zones in the drainage area range from Mediterranean to hyperarid, and fluctuate dramatically through glacial cycles (Bar-Matthews et al., 2003; Miebach et al., 2019). The region is characterized by a relatively dry climate during the Holocene and a humid climate during the Last Glacial. Consequently, the Holocene Dead Sea is at low-stand with higher salinity in contrast to high-stand conditions with lower salinity during the Last Glacial (Torfstein et al., 2013; Lazar et al., 2014). The current Dead Sea water

has a salinity of 340 ‰ (240 kg/m^3) ($\sim$9 times greater than seawater) and a density of 1240 kg/m^3 (Arnon et al., 2019). By comparison, the salinity and density of central-southern Lake Lisan water are estimated to be 70-130‰ (50-100 kg/m^3) and 1050-1100 kg/m^3, respectively (Begin et al., 2004; Lazar et al., 2014). Thermohaline stratification is observed in the Dead Sea during summer but disappears during winter (Arnon et al., 2019).

2.2. Flash flood and surface plume monitoring

Flash floods play a key role in sediment delivery and Dead Sea basin filling. Due to the sparse vegetative cover in the lake catchment, suspended sediment concentrations of flash floods in the region are extremely high (Cohen and Laronne, 2005). Suspended sediment concentrations of floods that occurred during the rainy season (winter) of 1997 and 2000 were measured near to river mouth of the Nahal Qanna'im-Rahaf (Fig. 1b). Among the seven measurements, one flood had a maximum sediment concentration of 270 kg/m^3; another three floods had maximum sediment concentrations >50 kg/m^3 (Cohen and Laronne, 2005).

Flood plumes are common in the lake during the rainy season and can reach the lake center (Fig. 1c-d). Surface water measurements near to the river mouths of Jordan River and the Nahal Qidron (Fig. 1b) after floods have revealed suspended particle concentrations decrease with distance offshore (Levy, 1981; Herut et al., 2002). Surface reflectance mapping of the entire Dead Sea through remote sensing applications following floods revealed that sediment concentrations are typically high along the shore and decrease with distance from shore (Fig. 1d) (Nehorai et al., 2013).
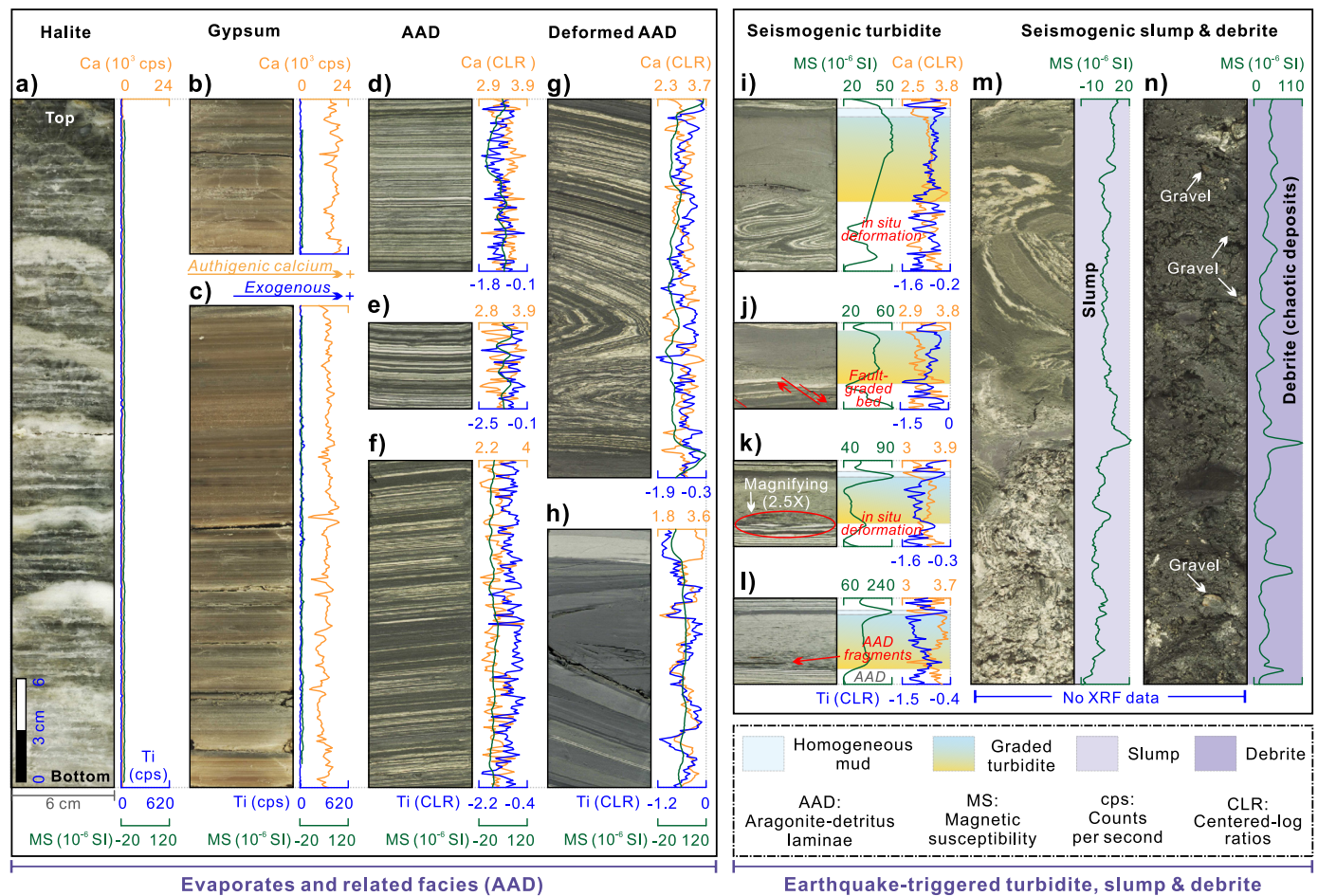
Fig. 2. Basic sediment facies in the ICDP Core 5017-1. a: Halite. b-c: Gypsum. d-f: AAD (Aragonite-detritus laminae). g-h: Earthquake-deformed AAD (Lu et al., 2020b). i-n, Seismogenic turbidites (Lu et al., 2021a), and seismogenic slump and chaotic deposits (Lu et al., 2017b). Depth of core intervals: (a), 24715-24755 cm; (b), 32751-32760 cm; (c), 33058-33086 cm; (d), 10578-10588 cm; (e), 11004.5-11009.5 cm; (f), 34024-34043 cm; (g), 33902-33924 cm; (h), 37515-37530 cm. (i), 14488-14499 cm; (j), 33499.5-33505.0 cm; (k), 11014-11019 cm; (l), 10914.5-10920 cm; (m), 12710-12744; (n), 15353-15387 cm. The vertical scale bar in (a) is valid for (b-n). All the core images have an aspect ratio of 1:1.

2.3. ICDP Core 5017-1 and previous lithofacies studies

The 457 m-long ICDP Core 5017-1 was drilled from the Dead Sea depocenter (31°30′29″ N, 35°28′16″ E) under a water depth of 297.5 m (lake level: −424 m) during 2010-2011. A hydraulic piston coring tool was used to recover the upper 30 meters of the core, while the deeper sections were cored by using the rotating extended-nose bit coring system (Stein et al., 2011). The recovery rate is about 90% (Neugebauer et al., 2014). The sedimentary sequence covers the past 220 kyr and its age model is built on a combination of ^{14}C (Kitagawa et al., 2017) and U-Th (Torfstein et al., 2015) dating, and δ^{18}O stratigraphy correlation (Goldstein et al., 2020). The recovered sequence comprises seven basic facies which can be classified into four groups, (I) evaporites and related facies: halite, gypsum, and aragonite-detritus laminae (including *in situ* deformed ones) (Fig. 2), (II) slump facies (Fig. 2), (III) debrite facies (Figs. 2, 3) and graded turbidite facies (Figs. 2, 3), and (IV) homogeneous mud (Fig. 3).

Halite and gypsum deposits in the core imply a negative water balance, increasing salinity, and thus indicating a relatively arid climate (Torfstein et al., 2015; Kiro et al., 2016). The aragonite-detritus laminae couplet reflects the input of runoff freshwater and a relatively humid climate (Lu et al., 2017a, 2020a; Ben Dor et al., 2018). Furthermore, units of *in situ* deformed aragonite-detritus

laminae indicate seismic activity along the central Dead Sea Fault (Lu et al., 2020b).

Slumps are characterized by intensely folded and fragmented aragonite-detritus laminae without gravel or coarse sands (Fig. 2m). The debrites comprise two sub-types (I) cohesive muddy debrites (Fig. 2n), and (II) poorly-cohesive clean sandy debrites (Fig. 3d-g). Type I debrites are muds that contain gravel, intraclasts, and coarse sands that show poorly-sorted chaotic structures, which were previously named chaotic deposits (Lu et al., 2017a). Slumps and Type I debrites (chaotic deposits) have been identified as seismically-triggered deposits by temporal correlation with previously established earthquake records on the Dead Sea Margin (Lu et al., 2017a).

Homogeneous mud facies are characterized by massive clay-fine silts without aragonite lamina (pelagic sediments) or particle grading. Thousands of graded sandy and muddy turbidites are observed in the core. Some of them are overlying *in situ* seismites without intervening background sediments, and some are temporally correlated with historic earthquakes, and thus identified as seismogenic turbidites (Lu et al., 2021a). However, for the rest of the turbidites, all homogeneous muds, and clean sandy debrites, the trigger(s) is unclear. Here, we focus on these three types of deposits with unclear triggers, analyze their thickness and frequency, and compare them to climate proxies.
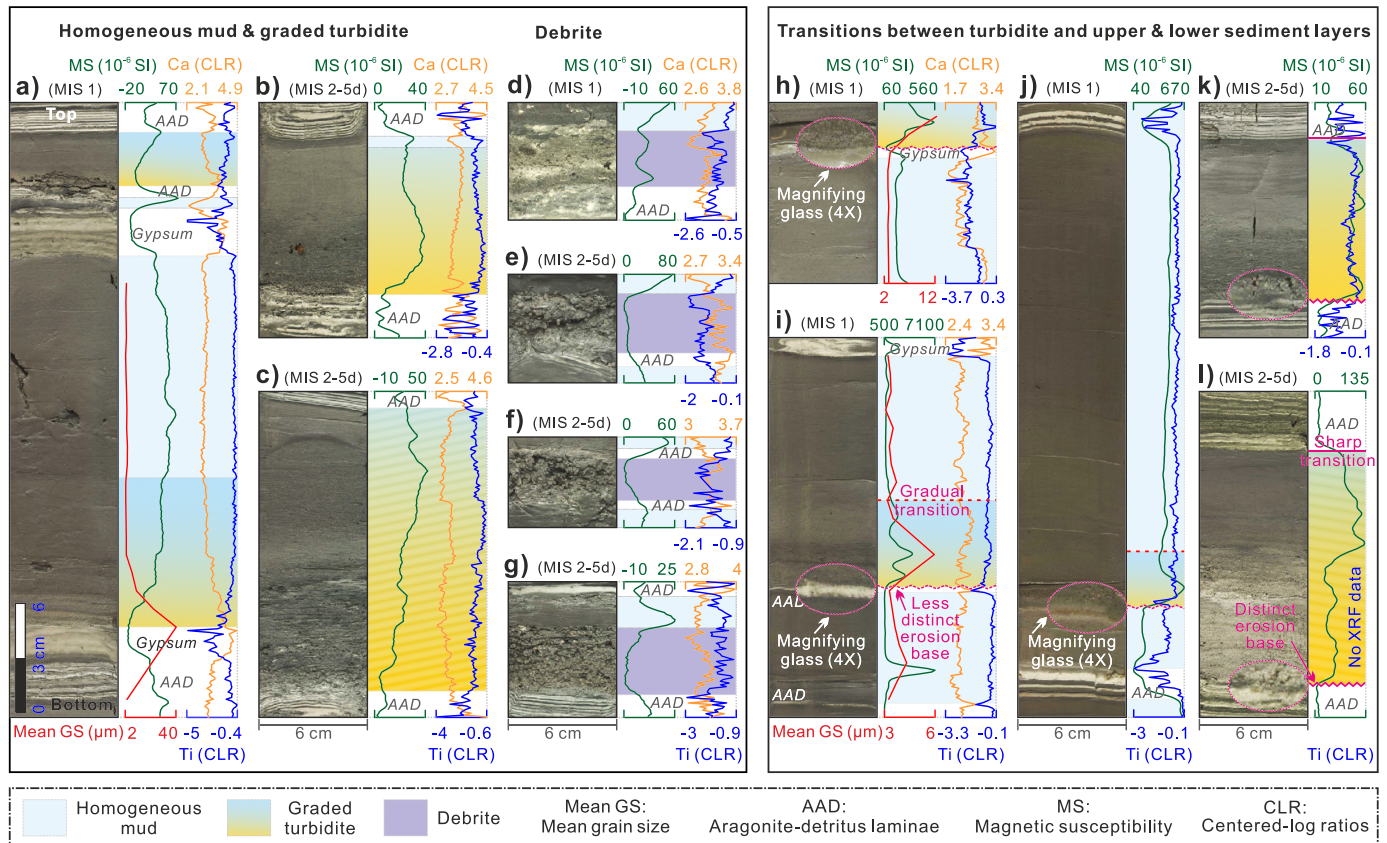
Fig. 3. Typical homogeneous mud, graded turbidite, and debrite with triggers unclear in the ICDP Core 5017-1. a-c, Homogeneous muds and graded turbidites. d-g, Debrites (See Fig. S1 for more examples). h-l, Core images showing different transitions between graded turbidite and upper and lower sediment layers in interglacial (h-j) and glacial (k, l). Depth of core intervals: (a), 8941-8975 cm; (b), 13940-13953 cm; (c), 17162.5-17180.5 cm; (d), 7863-7869.5 cm; (e), 16821.5-16827.5 cm; (f), 16917-16922 cm; (g), 17205.5-17213 cm; (h), 2097.5-2107.5 cm; (i), 2620-2641 cm; (j) 1391-1425 cm; (k), 11369-11382 cm; (l), 12941-12959 cm. The vertical scale bar in (a) is valid for (b-l). All the core images have an aspect ratio of 1:1.

2.4. Hypothesis

Climate in the Dead Sea area has changed substantially over glacial cycles. The lake was in a low-stand phase (< -380 m) with higher salinity ($\sim$300‰ or $\sim$200 kg/m^3) and water density ($\sim$1200 kg/m^3) during the Holocene. In contrast, it was in a high-stand condition (> -300 m), with lower salinity (70-130‰ or 50-100 kg/m^3) and water density (1050-1100 kg/m^3) during the Last Glacial (Begin et al., 2004; Lazar et al., 2014; Torfstein, 2019). In oceanic environments (salinity: $\sim$35‰ or 35 kg/m^3, ρ_{seawater}: $\sim$1025 kg/m^3), sediment concentrations of $\sim$40 kg/m^3 are required for river plumes to trigger turbidity currents at the river mouth directly (hyperpycnal plunging) (Mulder and Syvitski, 1995). Based on the threshold of 40 kg/m^3 assumed for oceanic environments, the threshold of sediment concentration of $\sim$200 kg/m^3 and $\sim$50-100 kg/m^3 are inferred for the Holocene and Last Glacial, respectively in the Dead Sea. It is therefore expected that overflows ($\rho_{\text{flow}} < \rho_{\text{water}}$) are more prominent during interglacials than in glacials, while underflows ($\rho_{\text{flow}} > \rho_{\text{water}}$) are more prominent during glacials. This paper will test this hypothesis by analyzing overflow and underflow sedimentation preserved in the high-resolution ICDP Core 5017-1 from the Dead Sea depocenter.

3. Methods

3.1. Magnetic susceptibility and XRF scanning

A Multi-Sensor Core Logger with a Bartington MS2E sensor was used for magnetic susceptibility logging at 1 mm resolution. Ele-

ment data at 1 mm resolution was obtained by ITRAX XRF scanning (equipped with a line-scan camera at GFZ Potsdam) using a Chromium tube at 30 kV voltage, 30 mA current, and exposure time of 1 s (Neugebauer et al., 2014). The high-resolution core images were also obtained during the non-destructive analyses. The abundance of titanium (Ti) and calcium (Ca) in the core have been used as proxies for clastic input and carbonate and gypsum, respectively (Lu et al., 2021a, 2021b). Here, we also use trends in these proxies to investigate sediment facies. Chloride (Cl) abundance was also used to indicate the relative variation of salinity since it can be linked to variability in halite content at orbital scales in the Dead Sea (Lazar et al., 2014). To counter the effects of grain size, water content, etc. and get a more reliable geochemical picture, we apply the method of centered-log ratios (CLR) to calibrate the intensity of Ti and Ca. The reliably measured elements of K, Ca, Ti, Fe, Cl, Ar, Br, and Sr are selected for geomean calculation and centered-log ratios transformation (Weltje et al., 2015). The method is not applicable to core intervals of halite and gypsum since the content of Ti is around 0 (Fig. 2a-c).

3.2. Grain size

Several representative intervals of homogeneous muds and graded turbidites from the core were chosen for grain size measurement at 1 cm intervals. The total organic carbon content of homogeneous mud layers and turbidites from the ICDP Core 5017-1 is generally between 0.3% and 1% (Neugebauer et al., 2016). Samples are pre-treated with H$_2$O$_2$ to remove organic matter (Konert and Vandenberghe, 1997; Lu et al., 2018), but without dissolu-

tion of carbonate minerals because remobilized calcite particles are common in the lake. The measurements were taken by using a Beckman-Coulter LS 230 laser particle sizer in the Environmental Sedimentology Lab at the University of Haifa.

3.3. Age calculation for sediment layers

We have noted that normally used event-free age modeling method is not feasible. This is because meter-thick energetic slumps and debrites are common in ICDP Core 5017-1. It is impossible to estimate the amount of eroded originally accumulated sediments at the drilling site (Lu et al., 2017a, 2021a). Thus, we apply linear interpolation to the age calculation of sediment layers between dated horizons. By using ^{14}C (Kitagawa et al., 2017), U-Th (Torfstein et al., 2015), and δ^{18}O stratigraphy correlation (Goldstein et al., 2020) methods, more than 50 dated horizons in the ICDP Core 5017-1 are available for age interpolation during the past 220 kyrs. The dated horizons have been previously summarized in Lu et al. (2020b) (Table S1).

4. Results

4.1. Characteristics of homogeneous muds, graded turbidites, and debrites (triggers unclear)

The different deposits are identified through their grain size, magnetic susceptibility, and chemical features. The units of homogeneous mud are composed of clay-fine silts (mean grain size <16 μm) without graded bedding. They show only relatively small variations in grain size, magnetic susceptibility, Ti and Ca (Fig. 3a, h, i). In contrast, the lower parts of graded turbidites are made up of coarse silts to fine sands and exhibit upward-fining particle sizes, increasing magnetic susceptibility and Ti, and large variations in Ca from bottom to top (Fig. 3a-c).

Thick intervals of homogeneous mud that exhibit sharp changes in magnetic susceptibility, Ti and Ca were interpreted as multiple sediment layers deposited in short succession, i.e. there was insufficient time between floods to deposit an identifiable thickness of the pelagic sediments (Fig. 4h-i). Low content of Ti and Ca, and small values in magnetic susceptibility characterize debrites that are composed of coarse sands and are predominantly ungraded (Fig. 3d-g). In total, we identify 3241 units of homogeneous mud, 1761 graded turbidites, and 39 debrites both with unclear triggers in the 457 m-long core.

4.2. Separating the unit of homogeneous mud from turbidite tail (T_E)

During interglacials, some graded turbidites are overlaid by thick homogeneous mud (Fig. 3a, i, j; Fig. 4). Typical units of homogeneous mud in the ICDP Core 5017-1 have only minor variations in grain size, magnetic susceptibility, Ti and Ca. In contrast, a gradual decrease or increase in grain size, magnetic susceptibility, Ti and Ca from graded bedding (T_A-T_D) to tail (T_E) of turbidites are expected. These key features are used to separate the unit of homogeneous mud from turbidite tail (Fig. 4a, c-d, h-i). In addition, according to the classical Bouma sequence (Bouma, 1962) and the revised Bouma sequence of Talling et al. (2012), the ratio between the thickness of turbidite tail (T_E) and graded bedding (T_A-T_D) is <1. In our Dead Sea case study, the typical units of overlying homogeneous mud are several times thicker than the graded bedding (T_A-T_D) and turbidite tail (T_E) of underlying turbidites (Fig. 4a, c-d, h-i), supporting our approach. We estimate the potential uncertainties in the thickness measurement for turbidite tails (T_E) are of minor importance when compared with the thickness of overlying thick units of homogeneous mud.

4.3. Records of homogeneous mud and graded turbidite compared to climate proxies

The Dead Sea 220 kyr-long record of sediment flow deposits comprises more than 5, 000 layers of homogeneous mud, graded turbidite, and debrites with unclear triggers. This is probably the largest dataset of sediment flow deposits that have ever been reported. The record of homogeneous mud and graded turbidite cover the MIS 7c-1, i.e. two glacial cycles (Fig. 5). The extremely long time span of record enables us to compare the return time and thickness of homogeneous mud and turbidite layers to orbital-scale climate changes (Fig. 5). The record of debrites was not compared to climate proxies due to a small number (N=39) of deposits layers.

The thicknesses of homogeneous muds (layers) range between 0.1 and 188 cm. Homogeneous muds are frequent (25-30 layers/kyr; Mean: 27) and thick (3-10 cm/layer; Mean: 5.9) during interglacials, and less frequent (8-12 layers/kyr; Mean: 10) and thinner (2-4 cm/layer; Mean: 3.3) during glacials (Fig. 5d-e; Table S2; Text S1). The thicknesses of graded turbidites range from 0.1 to 109 cm. Graded turbidites are frequent (7-14 layers/kyr; Mean: 10) but thin (2-4 cm/layer; Mean: 3.0) during interglacials, and less frequent (4-12 layers/kyr; Mean: 8) but thicker (3-5 cm/layer; Mean: 3.4) during glacials (Fig. 5f-g; Table S2; Text S1).

At orbital scales, over MIS 7-1, the periods with thick and frequent homogeneous muds correlate to interglacial low-stand phases with high salinity (Fig. 5a-e) and a higher sedimentation rate (Fig. S2). The periods with thicker graded turbidites correlate to glacial high-stand conditions with low salinity (Fig. 5f, g). Moreover, the variations in return time and thickness of homogeneous mud layer are generally following the change in the global benthic foraminiferal δ^{18}O stack and the Dead Sea salinity (Fig. 5a, b, d, e). The homogeneous mud layers are thicker and more frequent when the climate was warmer and water salinity was higher.

4.4. Thickness distribution of seven facies during individual glacials and interglacials

Halite units are mainly formed during interglacials, while gypsum and aragonite-detritus laminae are mainly deposited during glacials (Fig. 6). The fraction of homogeneous mud during interglacials (MIS7a-c: 49%, MIS5e: 45%, and MIS1: 52%) is much higher than during glacials (MIS6: 23% and MIS2-5d: 26%). In addition, the fraction of turbidites and debrites during glacials (MIS6: 44% and MIS2-5d: 24%) is much higher than during interglacials (MIS7a-c: 23%, MIS5e: 12%, and MIS1: 5%). Furthermore, during individual interglacials, the thickness fraction of homogeneous mud is one to ten times higher than turbidites and debrites (MIS7a-c: 49% *vs.* 23%, MIS5e: 45% *vs.* 12%, and MIS1: 52% *vs.* 5%). In contrast, during individual glacials, the fraction of turbidites and debrites is one to two times as much as homogeneous mud (MIS6: 44% *vs.* 23% and MIS2-5d: 24% *vs.* 26%).

5. Discussion

5.1. Linking deposits in geological record to sediment density flows

Field *in situ* measuring in the Dead Sea reveals that flash flood-generated overflows can reach the lake center, and sediment concentrations of 0.05-0.3 kg/m^3 were measured at 5 km offshore (Fig. 1b) (Nehorai et al., 2013). Moreover, sediment traps deployed in the lake center captured sediment accumulation rates of 17, 12, and 11 g/m^2/day at water depths of 70, 120, and 170 m following floods that occurred during February 9-March 8 1983, respectively (Fig. 1b, e) (Stiller et al., 1997). According to Stokes' Law, more time is needed for particles settling for a deeper water depth. The
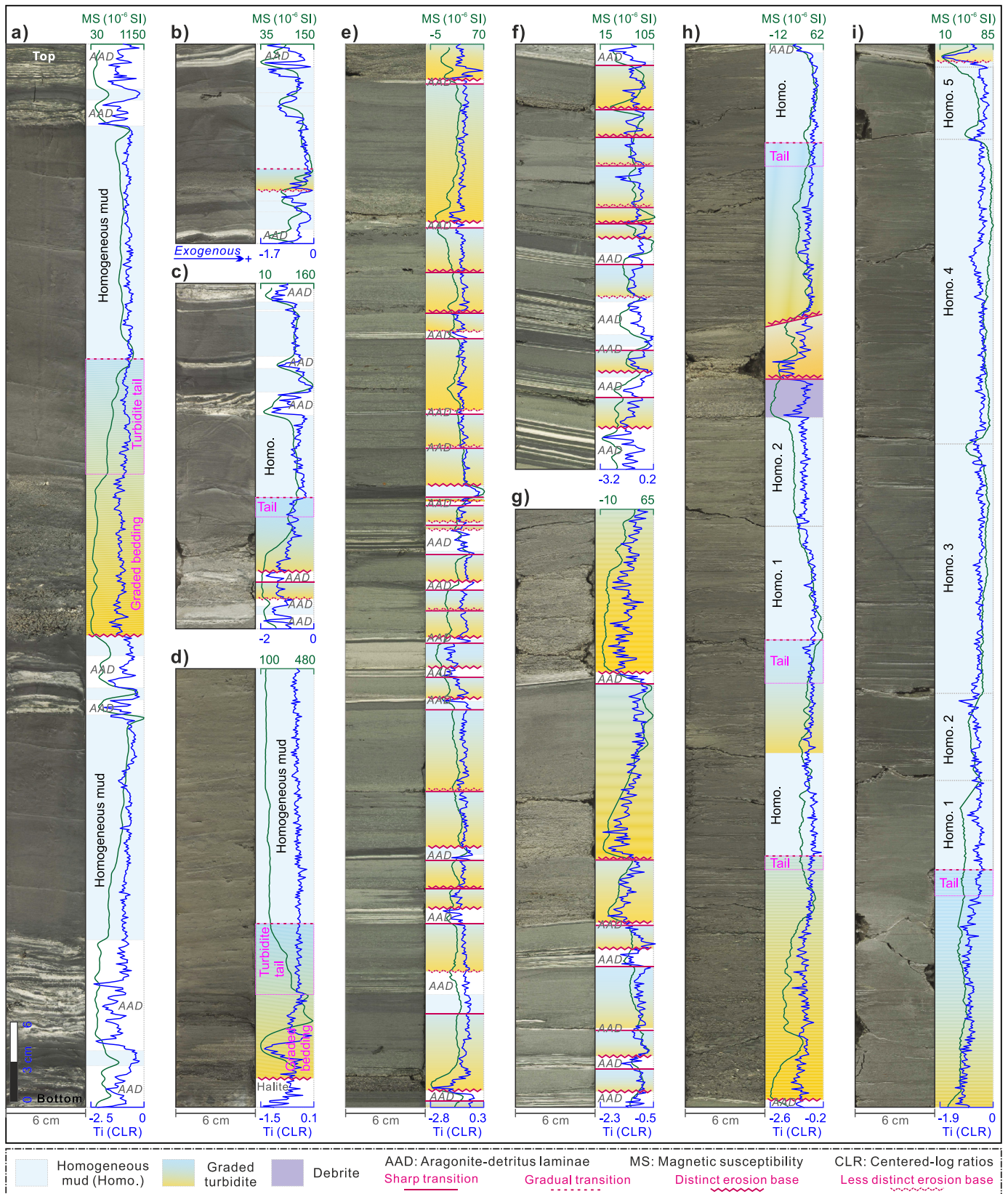
Fig. 4. Core images showing turbidite tails, different transitions between turbidite and upper and lower sediment layers, and multiple sediment layers in single thick interval of homogeneous mud. Core depth: (a), 21900-21980 cm; (b), 17515-17530 cm; (c), 18035-18061 cm; (d), 26680-26713 cm; (e), 32890-32970 cm; (f), 35828-35860 cm; (g), 36300-36345 cm; (h), 39994-40074 cm; (i), 42602-42682 cm. The vertical scale bar in (a) is valid for (b-i). All the core images have an aspect ratio of 1:1.
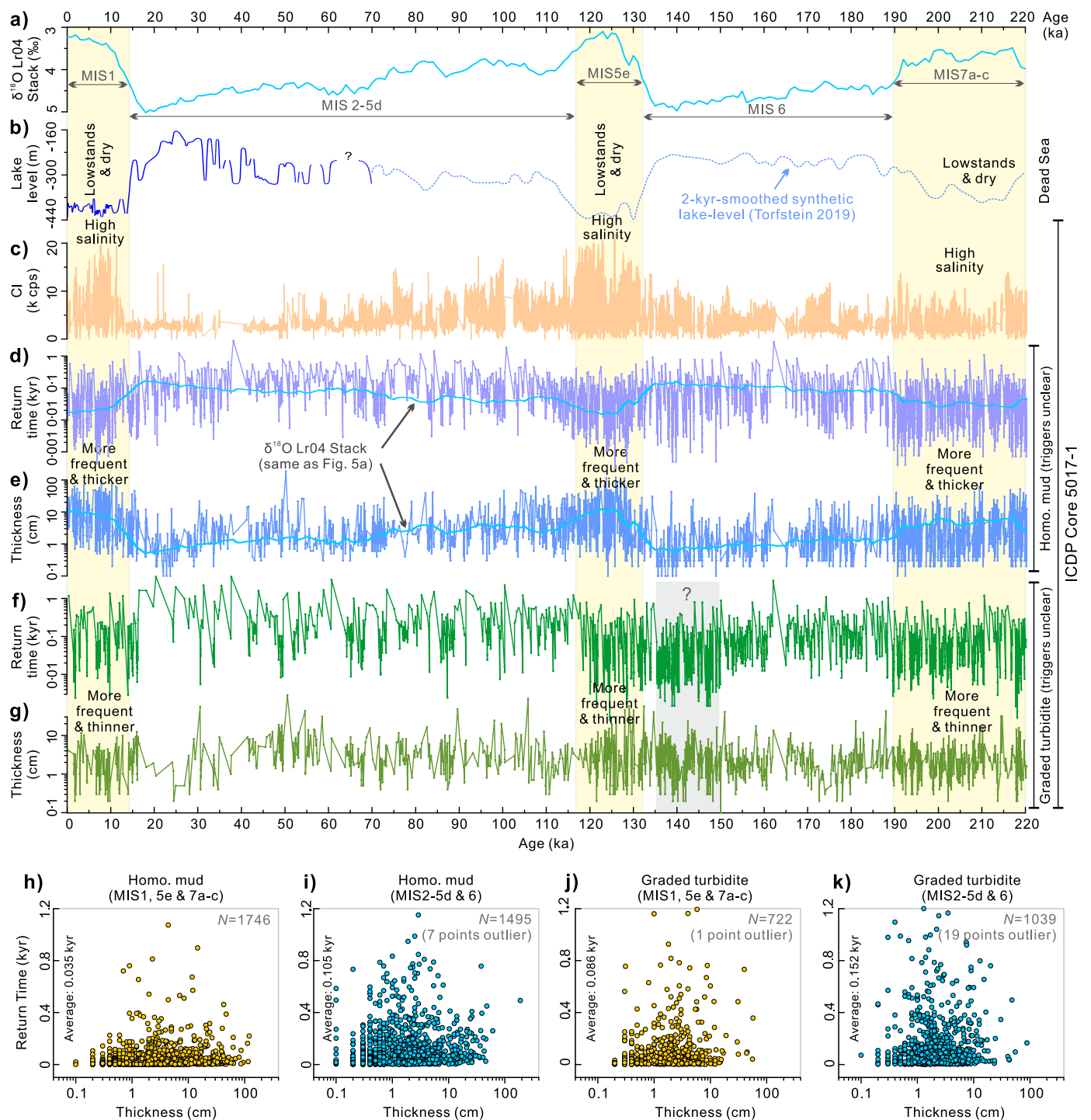
Fig. 5. Records of homogeneous (homo.) mud and graded turbidite (triggers unclear) from the ICDP Core 5017-1 compared to global and regional climate proxies. a, Global benthic foraminiferal $\delta^{18}O$ stack (Lisiecki and Raymo, 2005). b, Dead Sea lake-level (Bookman et al., 2006; Torfstein et al., 2013; Torfstein, 2019). c, Chloride (Cl) was used as a proxy of salinity (Lazar et al., 2014). d-e, Return time and thickness of homogeneous mud. f-g, Return time and thickness of graded turbidite. h-k, Return time and thickness distribution of homogeneous mud and graded turbidite during interglacials (h, j) and glacials (i, k).

decrease in sediment accumulation from 70 to 170 m water depth in a fixed time period indicates vertical settling of suspended clay-fine silts, which supports the interpretation that floods generate sediment-laden overflows that can reach the center of the hyper-saline lake. Flood-related surface plumes thus can represent a major process for delivering clay and fine silts to the lake depocenter. We therefore link the homogenous muds in the ICDP Core 5017-1 to flood-generated overflows. Flood-related sediment transport via interflows is considered negligible because the Dead Sea is not

stratified during winter (Arnon et al., 2019) when most floods occur in the catchment.

Previous studies have revealed that turbidity currents can be generated via three basic mechanisms, (a) plume settling (Lintern et al., 2016; Hage et al., 2019), (b) hyperpycnal river plunging (Mulder and Syvitski, 1995; Heerema et al., 2022), and (c) sub-aqueous slope failures (Piper and Savoye, 1993; Mulder et al., 1997). Laboratory experiments have suggested that turbidity currents can be triggered by surface plume settling (convective fin-
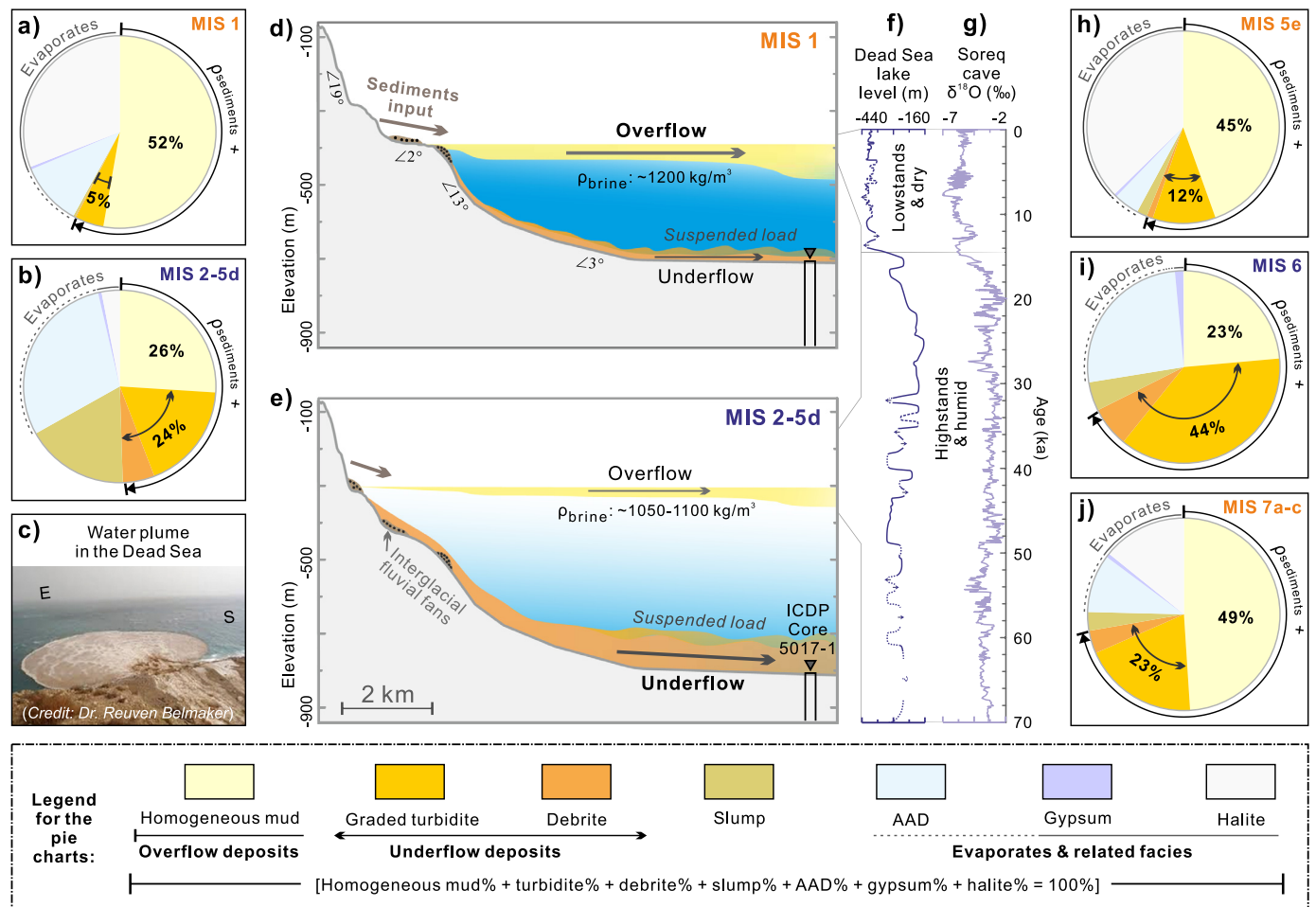
Fig. 6. Thickness distribution of seven facies (regardless of triggers) through glacial cycles and mechanisms for flow processes. a–b, Thickness distribution of facies during the last glacial cycle (Table 1). c, Flood plume on top of the dense Dead Sea brine. d–e, Schematic model illustrating mechanisms for flow processes under interglacial (d) and glacial (e) conditions. f: Lake-level (Bookman et al., 2006; Torfstein et al., 2013). g: $\delta^{18}O_{speleo}$ record from the Soreq Cave (Fig. 1a) (Grant et al., 2012). h–j, Thickness distribution of facies over MIS 7-5e.

gering) when sediment concentrations reach 1 kg/m³ (Parsons et al., 2001). This is significantly lower than the concentration required for hyperpycnal flows to occur (>40 kg/m³ when $\rho_{seawater}$: ~1025 kg/m³) (Mulder and Syvitski, 1995). However, other direct monitoring studies at a fjord-head delta in British Columbia, have shown that turbidity currents can be triggered by plume settling where concentrations are as low as 0.07 kg/m³ (Hage et al., 2019).

In the Dead Sea, sediment concentrations of 0.6-3.9 kg/m³ were measured for surface plumes at 50 m offshore (water depth: 9 m), following more intense floods feeding through Nahal Arugot (Fig. 1b) during February 29 and March 3, 2012 (Nehorai et al., 2013). Such concentration levels (>0.6 kg/m³) are estimated to be enough to generate turbidity currents in the Dead Sea (ρ_{brine}: ~1200 kg/m³) via the plume settling mechanism (oceanic: $\rho_{seawater}$: ~1025 kg/m³, concentration ≥0.07 kg/m³). Much higher sediment concentrations for the same floods are expected at the river mouth. In addition, suspended sediment concentrations of 50-270 kg/m³ have been previously measured near the river mouth of Nahal Rahaf-Qanna'im (Fig. 1b) (Cohen and Laronne, 2005). Such high sediment concentrations favor the triggering of turbidity currents via the hyperpycnal plunging mechanism. Hundreds of seismogenic turbidites resulting from subaqueous slope failures have been identified in the ICDP Core 5017-1 (Lu et al., 2021a). Debrites which containing gravel and sands in the core result from debris flows that relate to small delta failures which may be triggered by earthquake shaking (Lu et al., 2017a) or

other mechanisms. We thus link the graded turbidites and debrites in the core to underflows.

5.2. Testing hypothesis

The ICDP Core 5017-1 was drilled from the lake center and depocenter which receives sediments arriving from the shores surrounding the lake. The thickness of flow deposits preserved in such a core generally indicates the relative duration and magnitude of sediment flows, and thus their total capacity for transporting sediments (Kämpf et al., 2015). The prominence of thicker, more frequent homogenous muds which make up a high proportion of clastic deposits during interglacials implies that overflows are more prominent during interglacials than in glacials. This is likely a consequence of the greater density of the lake brine during interglacials preventing floodwater from plunging and reducing the rate of suspended particle settling. Furthermore, the upper slopes of high-stand lakes during glacials which accumulated unconsolidated aragonite-detritus laminae, were exposed to erosion during interglacial low-stands. These fine-grained sediments are less likely to develop into underflows, but rather tend to support the development of overflows (surface plumes) during interglacials.

The greater proportion of turbidites and debrites during glacials suggests that underflows and the triggering of sediment gravity flows are more likely. The less-dense lake brine during glacials is more favorable for developing turbidity currents via hyperpycnal plunging and plume settling. In addition, the high-stand

Table 1
Thickness distribution of seven basic facies (regardless of triggers) through glacial cycles.

MIS stage	Homogeneous mud	Turbidite	Debrite	Slump	AAD*	Gypsum	Halite	Total
MIS 1	51.8%	4.7%	0.1%	0.3%	10.4%	0.4%	30.4%	100%
MIS 2-5d	26.0%	18.1%	5.4%	17.4%	29.5%	0.6%	3.0%	100%
MIS 5e	44.8%	10.7%	1.0%	1.7%	4.3%	0.5%	37.5%	100%
MIS 6	23.5%	37.1%	6.7%	4.8%	26.0%	1.4%	0.1%	100%
MIS 7a-c	49.0%	19.5%	3.8%	3.1%	9.8%	0.7%	14.2%	100%

Note: *AAD, aragonite-detritus laminae; including *in situ* deformed ones.

glacial lakes submerged steeper marginal slopes and preceding interglacial fluvial fans (Fig. 6d-e), making the triggering of slope failures that can transform downslope into debris flows and turbidity currents more likely (Lu et al., 2021b).

The deposit thickness comparison also suggests that the relative importance for sediment transport volumes varies between glacials and interglacials. During interglacials, homogeneous muds are >2 times thicker than turbidites and debrites but represent <50% of sedimentation during glacials (Fig. 6; Table 1). This also suggests that overflows dominate sediment transport to the basin depocenter during interglacials but this is reversed during glacials. Therefore, the long sediment core dataset confirmed our hypothesis.

5.3. Implications for mechanisms of turbidite generating over glacial cycles

During glacials, 60-90% of turbidites are graded sandy turbidites. The contact between such units and upper sediment layers is usually sharp rather than gradual (Fig. 3k, l; Fig. 4). These units always have distinct erosional bases. However, during interglacials, 50-70% of turbidites are graded muddy turbidites. These units are usually overlaid by thick homogeneous mud with gradual transitions (Fig. 3i, j; Fig. 4). Such units usually have less distinct erosion bases.

We infer that the hyperpycnal plunging mechanism is more dominant for generating turbidity currents during glacials when water salinity and density are lower (ρ_{water}: 1050-1100 kg/m^3). During these time periods, sand particles (>100 μm), which formed the lower parts of graded sandy turbidites, are more likely to be carried directly by hyperpycnal river plunging from the river mouth rather than by surface flood plumes. The role of the plume settling mechanism is thought to be minor in forming sand-rich turbidity currents during glacials.

In contrast, during interglacials when water salinity and density are higher (ρ_{water}: ~1200 kg/m^3), medium to coarse silts (<50 μm) that formed the lower parts of graded muddy turbidites can be carried by offshore surface plumes. This condition is favorable for developing turbidity currents via the plume settling mechanism. At the same time, the greater lake brine salinity and density could prevent floodwater from plunging and weakening the strength of hyperpycnal flows. Larger particle size, higher sediment concentration, and density are required to generate turbidity currents via the hyperpycnal plunging mechanism. The plume settling mechanism is inferred to be more dominant for generating turbidity currents during the interglacials. Consequently, more frequent but thinner turbidites are recorded during interglacials in the ICDP Core 5017-1 (Fig. 5f-g).

6. Wider implications

A better understanding of the linkages between modern sedimentary processes, sedimentary dynamics, and the stratigraphic record is essential for subaqueous paleoseismology and paleoclimate research. Our study bridges the gap between our understanding of modern sedimentary processes and the stratigraphic record

in a hypersaline lake. Dead Sea is a hypersaline lake in a tectonically active region (Dead Sea Rift Zone), as a result, the lake deposits were controlled by both climate change and geodynamic activity. It therefore has the potential to inform our wider understanding of turbidite paleoseismology as well as paleoclimatic reconstructions in tectonically active subaqueous environments.

6.1. Implications for turbidite paleoseismology

Turbidites from lake and ocean sediments located in tectonically active regions have been widely used for geohazard assessments (Goldfinger et al., 2007; Polonia et al., 2013; Moernaut et al., 2014; Hubert-Ferrari et al., 2020). The use of turbidites as a paleoearthquake indicator normally requires a demonstration that seismicity, rather than other factors (e.g., floods), is the most plausible trigger. However, it is common that prehistoric turbidites are used as a proxy without reliable demonstration that an earthquake is the most plausible trigger. Our present study shows that even in an active graben like the Dead Sea, the occurrence of turbidites in the sedimentary archive within a deep central depocenter is modulated by climate change and climate-driven factors (e.g., water level, water density).

Similar climate-driven cycles of turbidite deposition from tectonically active regions have also been found in marine settings. Studies from the Peru-Chile Trench (South-Chilean active margin) have identified reduced frequencies of turbidite deposition during interglacials (i.e. MIS 1 and MIS 5). The reduced frequency of turbidites, despite the seismically active nature of the region, is attributed to reduced export of terrestrial sediment to the continental slope as a consequence of interglacial sea level highs and onshore aridity (Blumberg et al., 2008; Bernhardt et al., 2015).

Nonetheless, long-term Turbidite paleoseismology records remain rare. Numerous studies have been carried out on marine (Goldfinger et al., 2007; Polonia et al., 2013; Howarth et al., 2021) and lacustrine (Moernaut et al., 2014; Ghazoui et al., 2019; Hubert-Ferrari et al., 2020) sediments. However, many of these do not extend beyond the Holocene. In many cases, the impacts of climate-driven changes to lake inputs (sediment delivery, water level etc.) on long-term turbidite frequency and therefore the sedimentation regime in which earthquakes are triggering slope failures remains unclear. Establishing the long-term record of changes of sediment dynamic processes therefore appears important when considering paleoseismicity records as this may impact the apparent frequency of turbidity currents triggered by large earthquakes. This underlines the value of comprehensive modern sediment flow monitoring to understand the role of different flow types in contrasting lacustrine and marine environments (Thunell et al., 1999; Hsu et al., 2008; Arai et al., 2013; Henry et al., 2021).

6.2. Implications for paleoclimate research

This study shows that variations in thickness and return period for homogeneous mud layers generally follow changes in the global benthic foraminiferal $\delta^{18}O$ stack during the past 220 kyrs (Fig. 5d, e). Homogeneous mud layers occur more frequently and are thicker when climate is warmer. They are less frequent and thinner when

climate is colder. This implies that the thickness and/or return period of homogeneous mud layers could be a promising proxy for paleoclimate reconstruction in hypersaline lake and ocean environments. Indeed, changes in the number and thickness of these deposits have the potential to inform our understanding of changes to processes which control sediment delivery to these environments as well as the nature of sedimentation.

In tectonically active subaqueous environments, like the Dead Sea Graben, turbidites and debrites that result from underflow deposits can be triggered by both climate-induced environmental changes and geodynamic activity (e.g., earthquakes and volcanic activity). Indeed, turbidites generated by different triggers have been reported in sedimentary archives which have been used for long-term climatic reconstructions, such as Lake Baikal (Russia) (Nelson et al., 1999), Lake Van (Turkey) (Stockhecke et al., 2014), and the Gulf of Corinth (De Gelder et al., 2022). In such environments, the overall thickness fraction of turbidites and debrites can be up to 10% of the entire drilled sequence. Paleoclimate reconstructions in these environments would therefore benefit from the removal of these instantaneous event deposits from the sediment sequence.

7. Conclusions

We present a large dataset of sediment flow deposits (N >5,000) from the 457 m-long and 220 kyr ICDP Core 5017-1 from the hypersaline Dead Sea depocenter. Homogeneous muds from the core were linked to overflows, and graded turbidites and debrites were linked to underflows. Orbital-scale climate change has affected the magnitude/frequency of sediment density flows via changing salinity and density profile of lake water, lake level, submerged area, and source materials. As a result, overflows are more prominent during interglacials, while underflows are more prominent during glacials. In addition, regarding the generating of turbidity currents, the hyperpycnal plunging mechanism is more dominant during glacials, while the plume settling mechanism is more dominant during interglacials.

The present research bridges the gap between our understanding of modern sediment density flow processes and deposits preserved in a long-term geological record in the Dead Sea, a tectonically active subaqueous environment (Dead Sea rift zone). It has wider implications for turbidite paleoseismology and implies that in some cases to develop prehistoric turbidites as a reliable paleoearthquake indicator, comprehensive modern sediment flow monitoring is essential. It also has wider implications for paleoclimate research in a tectonically active subaqueous environment. Firstly, the thickness and/or return period of homogeneous mud layers in hypersaline lake and ocean environments could be a promising proxy for paleoclimate. Secondly, a sedimentary archive is filtered to remove significant instantaneous event deposits such as thick turbidites and debrites could help paleoclimatologists to better reconstruct paleoclimate change.

CRediT authorship contribution statement

Yin Lu: Conceptualization, Analysis, Validation, Writing original draft, Funding acquisition, Project administration.
Ed L. Pope: Analysis, Validation, Review & editing.
Jasper Moernaut: Analysis, Validation, Review & editing, Funding acquisition.
Revital Bookman: Review & editing.
Nicolas Waldmann: Review & editing.
Amotz Agnon: Review & editing.
Shmuel Marco: Review & editing.
Michael Strasser: Analysis, Validation, Review & editing.

Declaration of competing interest

The authors declare that they have no known competing financial interests or personal relationships that could have appeared to influence the work reported in this paper.

Data availability

Datasets are available in the Supporting Information and PANGAEA database (https://doi.org/10.1594/PANGAEA.938454).

Appendix A. Supplementary material

Supplementary material related to this article can be found online at https://doi.org/10.1016/j.epsl.2022.117723.

References

Arai, K., Naruse, H., Miura, R., et al., 2013. Tsunami-generated turbidity current of the 2011 Tohoku-Oki earthquake. Geology 41 (11), 1195–1198. https://doi.org/10.1130/g34777.1.

Arnon, A., Brenner, S., Selker, J.S., et al., 2019. Seasonal dynamics of internal waves governed by stratification stability and wind: analysis of high-resolution observations from the Dead Sea. Limnol. Oceanogr. 64 (5), 1864–1882. https://doi.org/10.1002/lno.11156.

Bar-Matthews, M., Ayalon, A., Gilmour, M., et al., 2003. Sea-land oxygen isotopic relationships from planktonic foraminifera and speleothems in the Eastern Mediterranean region and their implication for paleorainfall during interglacial intervals. Geochim. Cosmochim. Acta 67 (17), 3181–3199. https://doi.org/10.1016/s0016-7037(02)01031-1.

Bartov, Y., Agnon, A., Enzel, Y., et al., 2006. Late Quaternary faulting and subsidence in the central Dead Sea basin. Isr. J. Earth-Sci. 55 (1), 17–31. https://doi.org/10.1560/E3RK-0RDY-3CUP-LN5A.

Begin, Z.B., Stein, M., Katz, A., et al., 2004. Southward migration of rain tracks during the last glacial, revealed by salinity gradient in Lake Lisan (Dead Sea rift). Quat. Sci. Rev. 23 (14–15), 1627–1636. https://doi.org/10.1016/j.quascirev.2004.01.002.

Belmaker, R., Lazar, B., Stein, M., et al., 2019. Constraints on aragonite precipitation in the Dead Sea from geochemical measurements of flood plumes. Quat. Sci. Rev. 221, 105876. https://doi.org/10.1016/j.quascirev.2019.105876.

Ben-Avraham, Z., Garfunkel, Z., Lazar, M., 2008. Geology and evolution of the southern Dead Sea Fault with emphasis on subsurface structure. Annu. Rev. Earth Planet. Sci. 36, 357–387.

Ben Dor, Y., Armon, M., Ahlborn, M., et al., 2018. Changing flood frequencies under opposing late Pleistocene eastern Mediterranean climates. Sci. Rep. 8 (1), 8445. https://doi.org/10.1038/s41598-018-25969-6.

Bernhardt, A., Melnick, D., Hebbeln, D., et al., 2015. Turbidite paleoseismology along the active continental margin of Chile – feasible or not? Quat. Sci. Rev. 120, 71–92. https://doi.org/10.1016/j.quascirev.2015.04.001.

Blumberg, S., Lamy, F., Arz, H.W., et al., 2008. Turbiditic trench deposits at the South-Chilean active margin: a Pleistocene–Holocene record of climate and tectonics. Earth Planet. Sci. Lett. 268 (3–4), 526–539. https://doi.org/10.1016/j.epsl.2008.007.

Bookman, R., Bartov, Y., Enzel, Y., et al., 2006. Quaternary lake levels in the Dead Sea basin: two centuries of research. Spec. Pap., Geol. Soc. Am. 401, 155–170.

Bouma, A.H., 1962. Sedimentology of Some Flysch Deposits: A Graphic Approach to Facies Interpretation. Elsevier, Amsterdam/New York.

Cohen, H., Laronne, J.B., 2005. High rates of sediment transport by flashfloods in the Southern Judean Desert, Israel. Hydrol. Process. 19 (8), 1687–1702. https://doi.org/10.1002/hyp.5630.

De Gelder, G., Doan, M.L., Beck, C., et al., 2022. Multi-scale and multi-parametric analysis of Late Quaternary event deposits within the active Corinth Rift (Greece). Sedimentology 69 (4), 1573–1598. https://doi.org/10.1111/sed.12964.

de Leeuw, J., Eggenhuisen, J.T., Cartigny, M.J.B., et al., 2018. Linking submarine channel-levee facies and architecture to flow structure of turbidity currents: insights from flume tank experiments. Sedimentology 65 (3), 931–951. https://doi.org/10.1111/sed.12411.

Ghazoui, Z., Bertrand, S., Vanneste, K., et al., 2019. Potentially large post-1505 AD earthquakes in western Nepal revealed by a lake sediment record. Nat. Commun. 10 (1), 2258.

Goldfinger, C., Morey, A.E., Nelson, C.H., et al., 2007. Rupture lengths and temporal history of significant earthquakes on the offshore and North coast segments of the Northern San Andreas Fault based on turbidite stratigraphy. Earth Planet. Sci. Lett. 254 (1–2), 9–27. https://doi.org/10.1016/j.epsl.2006.11.017.

Goldstein, S.L., Kiro, Y., Torfstein, A., et al., 2020. Revised chronology of the ICDP Dead Sea deep drill core relates drier-wetter-drier climate cycles to insolation over the past 220 kyr. Quat. Sci. Rev. 244, 106460. https://doi.org/10.1016/j.quascirev.2020.106460.

Grant, K.M., Rohling, E.J., Bar-Matthews, M., et al., 2012. Rapid coupling between ice volume and polar temperature over the past 150,000 years. Nature 491 (7426), 744–747. https://doi.org/10.1038/nature11593.

Greenbaum, N., Ben-Zvi, A., Haviv, I., et al., 2006. The hydrology and paleohydrology of the Dead Sea tributaries. Spec. Pap., Geol. Soc. Am. 401, 63–93.

Hage, S., Cartigny, M.J.B., Sumner, E.J., et al., 2019. Direct monitoring reveals initiation of turbidity currents from extremely dilute river plumes. Geophys. Res. Lett. 46 (20), 11310–11320. https://doi.org/10.1029/2019GL084526.

Hall, J.K., 1997. Topography and bathymetry of the Dead Sea Depression. In: Niemi, T.M., Ben-Avraham, Z., Gat, J. (Eds.), The Dead Sea: The Lake and Its Setting. Oxford Univ. Press, USA, pp. 11–21.

Heerema, C.J., Cartigny, M.J.B., Jacinto, R.S., et al., 2022. How distinctive are flood-triggered turbidity currents? J. Sediment. Res. 92 (1), 1–11. https://doi.org/10.2110/jsr.2020.168.

Henry, P., Özeren, S., Yakupoğlu, N., et al., 2021. Slow build-up of turbidity currents triggered by a moderate earthquake in the Sea of Marmara. Natural Hazards and Earth System Sciences Discussions: 1-28.

Herut, B., Gavrieli, I., Halicz, L., et al., 2002. Suspended particulate matter in the western Dead Sea: distribution and chemical composition. Isr. J. Earth-Sci. 51.

Howarth, J.D., Barth, N.C., Fitzsimons, S.J., et al., 2021. Spatiotemporal clustering of great earthquakes on a transform fault controlled by geometry. Nat. Geosci. 14 (5), 314–320.

Hsu, S.-K., Kuo, J., Chung-Liang, L., et al., 2008. Turbidity currents, submarine landslides and the 2006 Pingtung earthquake off SW Taiwan. Terr. Atmos. Ocean. Sci. 19 (6), 7.

Hubert-Ferrari, A., Lamair, L., Hage, S., et al., 2020. A 3800 yr paleoseismic record (Lake Hazar sediments, eastern Turkey): implications for the East Anatolian Fault seismic cycle. Earth Planet. Sci. Lett. 538, 116152.

Kämpf, L., Mueller, P., Höllerer, H., et al., 2015. Hydrological and sedimentological processes of flood layer formation in Lake Mondsee. Depos. Rec. 1 (1), 18–37. https://doi.org/10.1002/dep2.2.

Kiro, Y., Goldstein, S.L., Lazar, B., et al., 2016. Environmental implications of salt facies in the Dead Sea. Geol. Soc. Am. Bull. 128, 824–841. https://doi.org/10.1130/b31357.1.

Kitagawa, H., Stein, M., Goldstein, S.L., et al., 2017. Radiocarbon chronology of the DSDDP core at the deepest floor of the Dead Sea. Radiocarbon 59 (2), 383–394.

Konert, M., Vandenberghe, J., 1997. Comparison of laser grain size analysis with pipette and sieve analysis: a solution for the underestimation of the clay fraction. Sedimentology 44 (3), 523–535.

Lamb, M.P., McElroy, B., Kopriva, B., et al., 2010. Linking river-flood dynamics to hyperpycnal-plume deposits: experiments, theory, and geological implications. Geol. Soc. Am. Bull. 122 (9–10), 1389–1400. https://doi.org/10.1130/b30125.1.

Lazar, B., Sivan, O., Yechieli, Y., et al., 2014. Long-term freshening of the Dead Sea brine revealed by porewater Cl− and in ICDP Dead Sea deep-drill. Earth Planet. Sci. Lett. 400, 94–101. https://doi.org/10.1016/j.epsl.2014.03.019.

Levy, Y., 1981. Suspended matter in the Dead Sea. Report No. MG/1981. The Geological Survey of Israel, Jerusalem, Israel.

Lintern, D.G., Hill, P.R., Stacey, C., et al., 2016. Powerful unconfined turbidity current captured by cabled observatory on the Fraser River delta slope, British Columbia, Canada. Sedimentology 63 (5), 1041–1064. https://doi.org/10.1111/sed.12262.

Lisiecki, L.E., Raymo, M.E., 2005. A Pliocene-Pleistocene stack of 57 globally distributed benthic $\delta^{18}O$ records. Paleoceanography 20 (1), PA1003. https://doi.org/10.1029/2004pa001071.

Liu, J.P., Kuehl, S.A., Pierce, A.C., et al., 2020. Fate of Ayeyarwady and Thanlwin Rivers Sediments in the Andaman Sea and Bay of Bengal. Mar. Geol. 423, 106137. https://doi.org/10.1016/j.margeo.2020.106137.

Lu, Y., Bookman, R., Waldmann, N., et al., 2020a. A 45 kyr laminae record from the Dead Sea: implications for basin erosion and floods recurrence. Quat. Sci. Rev. 229, 106143. https://doi.org/10.1016/j.quascirev.2019.106143.

Lu, Y., Fang, X., Friedrich, O., et al., 2018. Characteristic grain-size component - A useful process-related parameter for grain-size analysis of lacustrine clastics? Quat. Int. 479, 90–99. https://doi.org/10.1016/j.quaint.2017.07.027.

Lu, Y., Moernaut, J., Bookman, R., et al., 2021a. A new approach to constrain the seismic origin for prehistoric turbidites as applied to the Dead Sea Basin. Geophys. Res. Lett. 48 (3). https://doi.org/10.1029/2020GL090947.

Lu, Y., Moernaut, J., Waldmann, N., et al., 2021b. Orbital- and millennial-scale changes in lake-levels facilitate earthquake-triggered mass failures in the Dead Sea Basin. Geophys. Res. Lett. 48 (14). https://doi.org/10.1029/2021GL093391.

Lu, Y., Waldmann, N., Ian Alsop, G., et al., 2017a. Interpreting soft sediment deformation and mass transport deposits as seismites in the Dead Sea depocenter. J. Geophys. Res., Solid Earth 122, 8305–8325. https://doi.org/10.1002/2017JB014342.

Lu, Y., Waldmann, N., Nadel, D., et al., 2017b. Increased sedimentation following the Neolithic Revolution in the Southern Levant. Glob. Planet. Change 152, 199–208. https://doi.org/10.1016/j.gloplacha.2017.04.003.

Lu, Y., Wetzler, N., Waldmann, N., et al., 2020b. A 220,000-year-long continuous large earthquake record on a slow-slipping plate boundary. Sci. Adv. 6 (48). https://doi.org/10.1126/sciadv.aba4170.

Maier, K.L., Gales, J.A., Paull, C.K., et al., 2019. Linking direct measurements of turbidity currents to submarine canyon-floor deposits. Front. Earth Sci. 7. https://doi.org/10.3389/feart.2019.00144.

Miebach, A., Stolzenberger, S., Wacker, L., et al., 2019. A new Dead Sea pollen record reveals the last glacial paleoenvironment of the southern Levant. Quat. Sci. Rev. 214, 98–116. https://doi.org/10.1016/j.quascirev.2019.04.033.

Moernaut, J., Daele, M.V., Heirman, K., et al., 2014. Lacustrine turbidites as a tool for quantitative earthquake reconstruction: new evidence for a variable rupture mode in south central Chile. J. Geophys. Res., Solid Earth 119 (3), 1607–1633. https://doi.org/10.1002/2013jb010738.

Mulder, T., Savoye, B., Syvitski, J., 1997. Numerical modelling of a mid-sized gravity flow: the 1979 Nice turbidity current (dynamics, processes, sediment budget and seafloor impact). Sedimentology 44 (2), 305–326.

Mulder, T., Syvitski, J.P., 1995. Turbidity currents generated at river mouths during exceptional discharges to the world oceans. J. Geol. 103 (3), 285–299.

Nehorai, R., Lensky, I.M., Hochman, L., et al., 2013. Satellite observations of turbidity in the Dead Sea. J. Geophys. Res., Oceans 118 (6), 3146–3160. https://doi.org/10.1002/jgrc.20204.

Nelson, C.H., Karabanov, E.B., Colman, S.M., et al., 1999. Tectonic and sediment supply control of deep rift lake turbidite systems: Lake Baikal, Russia. Geology 27 (2), 163–166.

Neugebauer, I., Brauer, A., Schwab, M.J., et al., 2014. Lithology of the long sediment record recovered by the ICDP Dead Sea Deep Drilling Project (DSDDP). Quat. Sci. Rev. 102, 149–165. https://doi.org/10.1016/j.quascirev.2014.08.013.

Neugebauer, I., Schwab, M.J., Waldmann, N.D., et al., 2016. Hydroclimatic variability in the Levant during the early last glacial (∼117-75 ka) derived from microfacies analyses of deep Dead Sea sediments. Clim. Past 12 (1), 75–90. https://doi.org/10.5194/cp-12-75-2016.

Parsons, J.D., Bush, J.W., Syvitski, J.P., 2001. Hyperpycnal plume formation from riverine outflows with small sediment concentrations. Sedimentology 48 (2), 465–478.

Piper, D.J., Savoye, B., 1993. Processes of late Quaternary turbidity current flow and deposition on the Var deep-sea fan, North-West Mediterranean Sea. Sedimentology 40 (3), 557–582.

Polonia, A., Panieri, G., Gasperini, L., et al., 2013. Turbidite paleoseismology in the Calabrian Arc Subduction Complex (Ionian Sea). Geochem. Geophys. Geosyst. 14 (1), 112–140. https://doi.org/10.1029/2012gc004402.

Pope, E.L., Talling, P.J., Carter, L., et al., 2017. Damaging sediment density flows triggered by tropical cyclones. Earth Planet. Sci. Lett. 458, 161–169. https://doi.org/10.1016/j.epsl.2016.10.046.

Stein, M., 2001. The sedimentary and geochemical record of Neogene-Quaternary water bodies in the Dead Sea Basin-inferences for the regional paleoclimatic history. J. Paleolimnol. 26 (3), 271–282.

Stein, M., Ben-Avraham, Z., Goldstein, S., et al., 2011. Deep drilling at the Dead Sea. Sci. Drill. 11, 46–47.

Stiller, M., Gat, J.R., Kaushansky, P., 1997. Halite precipitation and sediment deposition as measured in sediment traps deployed in the Dead Sea: 1981-1983. In: Niemi, T.M., Ben-Avraham, Z., Gat, J. (Eds.), The Dead Sea: The Lake and Its Setting. Oxford Univ. Press, USA, pp. 171–183.

Stockhecke, M., Sturm, M., Brunner, I., et al., 2014. Sedimentary evolution and environmental history of Lake Van (Turkey) over the past 600,000 years. Sedimentology 61 (6), 1830–1861. https://doi.org/10.1111/sed.12118.

Sturm, M., Matter, A., 1978. Turbidites and varves in Lake Brienz (Switzerland): deposition of clastic detritus by density currents. In: Modern and Ancient Lake Sediments, pp. 147–168.

Talling, P.J., Masson, D.G., Sumner, E.J., et al., 2012. Subaqueous sediment density flows: depositional processes and deposit types. Sedimentology 59 (7), 1937–2003. https://doi.org/10.1111/j.1365-3091.2012.01353.x.

Thunell, R., Tappa, E., Varela, R., et al., 1999. Increased marine sediment suspension and fluxes following an earthquake. Nature 398 (6724), 233–236.

Thunell, R.C., Williams, D.F., 1989. Glacial–Holocene salinity changes in the Mediterranean Sea: hydrographic and depositional effects. Nature 338 (6215), 493–496.

Torfstein, A., 2019. Climate cycles in the southern Levant and their global climatic connections. Quat. Sci. Rev. 221, 105881. https://doi.org/10.1016/j.quascirev.2019.105881.

Torfstein, A., Goldstein, S.L., Kushnir, Y., et al., 2015. Dead Sea drawdown and monsoonal impacts in the Levant during the last interglacial. Earth Planet. Sci. Lett. 412, 235–244. https://doi.org/10.1016/j.epsl.2014.12.013.

Torfstein, A., Goldstein, S.L., Stein, M., et al., 2013. Impacts of abrupt climate changes in the Levant from Last Glacial Dead Sea levels. Quat. Sci. Rev. 69, 1–7. https://doi.org/10.1016/j.quascirev.2013.02.015.

Van Rooij, D., 2004. An integrated study of Quaternary sedimentary processes on the eastern slope of the Porcupine Seabight, SW of Ireland. Doctoral dissertation, Ghent University, Ghent, Belgium. 330 pp.

Weltje, G.J., Bloemsma, M., Tjallingii, R., et al., 2015. Prediction of geochemical composition from XRF core scanner data: a new multivariate approach including automatic selection of calibration samples and quantification of uncertainties. In: Micro-XRF Studies of Sediment Cores. Springer, pp. 507–534.

Zhang, Y., Liu, Z., Zhao, Y., et al., 2018. Long-term in situ observations on typhoon-triggered turbidity currents in the deep sea. Geology 46 (8), 675–678. https://doi.org/10.1130/g45178.1.